optica

Soft x-ray imaging spectroscopy with micrometer resolution

Jan O. Schunck,[1,2] Florian Döring,[3] Benedikt Rösner,[3] Jens Buck,[4,5] Robin Y. Engel,[1,2] Piter S. Miedema,[1] Sanjoy K. Mahatha,[1] Moritz Hoesch,[1] Adrian Petraru,[6] Hermann Kohlstedt,[6] Christian Schüssler-Langeheine,[7] Kai Rossnagel,[1,4,5] Christian David,[3] and Martin Beye[1,2,*]

[1]Deutsches Elektronen-Synchrotron DESY, 22607 Hamburg, Germany
[2]Department of Physics, Universität Hamburg, 22761 Hamburg, Germany
[3]Paul Scherrer Institut, 5232 Villigen PSI, Switzerland
[4]Institut für Experimentelle und Angewandte Physik, Christian-Albrechts-Universität zu Kiel, 24098 Kiel, Germany
[5]Ruprecht Haensel Laboratory, Kiel University and DESY, 24098 Kiel and 22607 Hamburg, Germany
[6]Nanoelektronik, Technische Fakultät, Christian-Albrechts-Universität zu Kiel, 24143 Kiel, Germany
[7]Helmholtz-Zentrum Berlin für Materialien und Energie, 12489 Berlin, Germany
*Corresponding author: martin.beye@desy.de

Received 27 August 2020; revised 18 December 2020; accepted 20 December 2020 (Doc. ID 405977); published 29 January 2021

Soft x-ray spectroscopy is invaluable for gaining insight into quantum materials. However, it is typically conducted in a spatially averaging way, making it blind to inhomogeneity in samples. Here, we demonstrate how we couple imaging to x-ray absorption spectroscopy and resonant inelastic x-ray scattering. Accordingly, we use a 2D detector and an off-axis Fresnel zone plate that images the sample in one spatial dimension and provides spectroscopic information in the other dimension. With our setup, we envision to enable a more detailed understanding of how the behavior of microscopic domains determines the functionality of quantum materials.

https://doi.org/10.1364/OPTICA.405977

1. INTRODUCTION

Functionality in quantum materials is driven by a delicate balance of contributions from different interacting degrees of freedom: the electronic subsystem with different spin arrangements, orbital occupations or charge distributions, and the lattice contributions [1,2]. This interplay can yield a variety of energetically close-lying states. Therefore, it is relatively easy to switch between different states by tuning external parameters such as temperature, pressure, or chemical composition. Together with chemical inhomogeneity, pinning centers, crystal defects, or even spontaneously forming phase separation, such an energetic environment is prone to form microscopic domains with distinct electronic properties. The macroscopic functionality is a result of the detailed combination of different local situations together with their spatial arrangement [3].

Some recent work highlights the importance of studying electronic properties on microscopic length scales to understand the macroscopic properties. Important spatially varying textures have been observed in various quantum materials, such as in the high-T_c superconductor $HgBa_2CuO_{4+y}$ [4], in the titanate compound $Y_{0.63}Ca_{0.37}TiO_3$ [5], and also in vanadium dioxide (VO_2), the well-known material with an insulator–metal transition near room temperature [6–9].

Modern soft x-ray spectroscopy methods, such as x-ray absorption spectroscopy (XAS) and resonant inelastic x-ray scattering (RIXS), provide a highly selective way to study fundamental properties of materials [10,11]. However, these methods often do not resolve microscopic domains in solids. If these methods are applied to inhomogeneous samples, an average response from all electronic domains under x-ray illumination is measured. Therefore, it is highly desirable to achieve microscopic spatial resolutions with XAS and RIXS. Typically, during RIXS measurements, x-ray energies emitted from the sample are recorded for a set of incident energies, which is commonly referred to as "RIXS maps." Such a measurement can be parallelized if the set of excitation energies produces spectra at different positions on a two-dimensional detector. The most natural realization of this concept is the combination of spatially dispersed radiation on the sample with an imaging spectrometer, allowing to record entire RIXS maps of homogeneous samples in one exposure. Such a setup additionally allows studying inhomogeneous samples with high spatial resolution. Several approaches in the soft [12–15] and hard [16] x-ray regime have been conceptualized. Most proposed realizations combine multiple mirrors and a grating.

In this work, we present a RIXS-imaging setup that allows measuring XAS in partial fluorescence yield and RIXS with a

spatial resolution down to 1.8 μm over a field of view of nearly 1 mm. Spectral and spatial information is simultaneously recorded and mapped onto the two dimensions of a CCD detector using the chromatic imaging properties of a transmission off-axis analyzer zone plate (AZP). The zone plate is the only optical element between the sample and detector. Its alignment is straightforward [17], limited to the one-dimensional positioning of the AZP along the optical axis to within several hundred micrometers. The RIXS-imaging concept is based on previous work presenting considerations concerning the energy resolution of an AZP-based spectrometer [18] as well as first spatially resolved measurements [17]. Here, we present an advanced setup that uses a second transmission zone plate upstream of the sample and a substantially larger sample magnification to achieve a peak spatial resolution of 1.8 μm, and we explain how we are able to record spectral and spatial resolution within a single measurement. This achievement paves the way to a more detailed understanding of the behavior of quantum materials on the microscale [19].

For the use of the RIXS-imaging setup, it is essential to understand the focal properties of zone plates and the behavior of spatial and energy resolution for energies that are in and out of focus on the detector. The focal length of a zone plate is approximately proportional to the diffracted photon energy (see Supplement 1). To estimate how wide the sufficiently resolved energy range in an AZP experiment is, one has to define the accepted limits of spatial and energetic resolution for energies ΔE that deviate from the energy at the optimal focus. This in turn determines the bandwidth $2\Delta E$ of emitted radiation that can effectively be recorded at the same time. Setting the AZP to focus the photon energy E_0 onto the detector results in a larger and defocused spot for an energy $E' = E_0 + \Delta E$. The spatial resolution on the sample $\Delta x_{\mathrm{Sample}}$ and the energy resolution dE for a small deviation ΔE from the focus energy E_0 are given by

$$\Delta x_{\mathrm{Sample}} = w \frac{\Delta E}{E_0} \cdot \frac{M+1}{M}, \tag{1}$$

$$dE = \frac{w}{\bar{r}} \cdot \Delta E. \tag{2}$$

Here, $w = r_{\mathrm{out}} - r_{\mathrm{in}}$ is the (radial) width of the off-axis zone plate, M is the magnification, and $\bar{r} = (r_{\mathrm{out}} + r_{\mathrm{in}})/2$ is the mean AZP radius. The derivation is sketched in Supplement 1, which expands on [18]. For example, when the used AZP is set to focus $E_0 = 530$ eV, for an energy offset of $\Delta E = 1$ eV, the spatial resolution degrades to 6.2 μm, and the energy resolution to 0.94 eV (see also Table S1). Both values increase mostly linearly for larger energy offsets. This chromatic defocusing contribution to spatial and energy resolution adds to contributions from detector, x-ray beam, the quality and alignment of the zone plates, and, ultimately, the diffraction limit [18] and becomes dominant for energies away from the center energy. Close to the focus, we measure a spatial resolution of 1.8 μm (see below), and estimate an energy resolution to 0.35 eV. Applying the formulas in [18] yields a similar result.

2. EXPERIMENT

The measurements are performed using the ultra-high vacuum endstation MUSIX [20] at the soft x-ray beamline P04 [21] at PETRA III, DESY in Hamburg. In our RIXS-imaging setup, the entire dispersed beam provided by the beamline is used to form a vertical line focus on the sample. Along this line, the sample

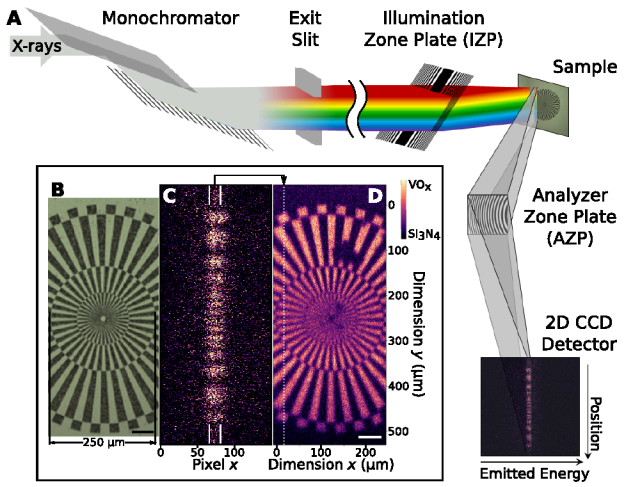

Fig. 1. (A) Schematic experimental setup and (B), (C) determination of spatial resolution. (A) A linear illumination zone plate and beamline components are used to create a sub-micrometer-wide and ∼970 μm long x-ray line focus on the sample. An off-axis Fresnel zone plate between sample and detector images the sample in direction of the focus line and disperses emitted x-rays in perpendicular direction. (B) Microstructured VO_x on Si_3N_4 Siemens star sample for spatial resolution characterization as seen by an optical microscope. (C) The line focus at the highlighted position in (D) excites oxygen K-edge fluorescence, yielding the shown image (background subtracted). (D) The vertical focus line is scanned across the Siemens star in horizontal direction, and the signal is integrated along the horizontal direction between the white lines indicated at top and bottom in (C). Scale bars are 50 μm.

is imaged and magnified onto the detector. The perpendicular direction on the detector is used to spectrally analyze x-ray emission from the sample. The RIXS-imaging setup can be applied in various modes that require a measurement strategy different from more conventional setups: (1) for heterogeneous samples and rather featureless spectra (e.g., fluorescence), the focus line and an orthogonal unidirectional scan can be used to map the sample structure; (2) for homogeneous samples, a so-called RIXS map (inelastic scattering spectra for a set of excitation energies) can be recorded in-parallel without any scan; (3) for heterogeneous samples with complex spectra, by scanning the sample surface as well as the excitation energy, high-dimensional information can be recorded, as will be described in more detail below. For both spatial mapping and energy analysis, the horizontal width of the line focus is required to be very small for optimal resolution. For this purpose, we refocus the incident x-rays horizontally with a linear transmission illumination zone plate (IZP) serving as cylindrical lens (Fig. 1A).

The monochromator of beamline P04 disperses x-rays vertically. We use a 400 line · mm^{-1} grating with a fix-focus constant c_{ff} of 1.6 [21], yielding a dispersion of 1.25 eV · mm^{-1} in the exit slit plane at a photon energy of 530 eV. A bandwidth of 3.6 eV is transported onto the sample, if we open the exit slits as far as possible (2.9 mm). Importantly, this broad bandwidth does not affect the RIXS energy resolution in our setup, but provides a range of excitation energies that can be detected in-parallel and permits utilizing a substantially higher fraction of the produced photon flux in comparison to working with a narrow bandwidth. The refocusing mirrors of beamline P04, located between the exit slit and the IZP (for clarity, not shown in Fig. 1), demagnify the exit

slit by a factor of three in the vertical direction. On the sample, the x-ray line focus thus measures approximately 970 μm vertically.

Horizontally, the refocusing mirrors are set to quasi-collimate the beam. The IZP has an aperture of 3.8 mm × 1.9 mm (v × h) and a focal length of 149.3 mm at an x-ray energy of 530 eV (see also Supplement 1). The first-order diffraction efficiency is around 5%–10%. Nanopositioning stages (SmarAct GmbH) allow for motion of the IZP in all three spatial dimensions, as well as tilt around a horizontal axis (perpendicular to the incident beam). This tilt is used as compensation for the chromatic behavior of the IZP: when changing the central incident photon energy, the IZP position along the beam is adapted to keep the focus on the sample. Two motorized baffles between IZP and sample serve as order sorting apertures.

In the spectrometer, the use of the transmission off-axis Fresnel zone plate allows to resolve spatial and spectral information from the sample at the same time [17,22]. The AZP has a size and aperture of 3 mm × 3 mm. The outer radius and outermost zone width are 4.7 mm and 35 nm, respectively. At a photon energy of 530 eV, the focal length is 140.7 mm. The first-order diffraction efficiency is approximately 10%–15%. The AZP is oriented to disperse x-rays in the horizontal and image in the vertical (direction of line focus). Both IZP and AZP are supported by a 100 nm thin silicon nitride membrane (see Supplement 1). This can cause apparent spectral variations for measurements in close proximity of the nitrogen and silicon absorption edges. For such measurements, pure silicon and carbon-based membranes should be used. Like the IZP, the AZP is also mounted on 3D nanopositioning stages for alignment and focus optimization. To focus different parts of the emission spectrum onto the detector, the AZP is moved along the sample–detector axis.

The detector is a direct detection CCD camera (Andor iKon-M) with a pixel size of $(13\ \mu m)^2$. The AZP is positioned at an object distance of 0.15 m and an image distance of 1.725 m, resulting in a magnification of 11.5. This enables us to achieve micrometer resolution. The camera is shielded from visible light with a 200 nm thin aluminum filter.

3. RESULTS

We used a Siemens star test structure to determine the overall spatial resolution of the setup. An optical microscopy image of this star is shown in Fig. 1(B). The star has a diameter of 500 μm and 72 spokes that consist of an oxide of vanadium (VO_x) deposited on silicon nitride (Si_3N_4). During the measurements, the angle of the sample normal in the horizontal scattering plane is 30° w.r.t the incident beam and 60° w.r.t the direction towards the detector.

The observed contrast arises from excitation of oxygen K-edge fluorescence in the VO_x containing parts of the Siemens star. With a beamline energy setting of 533 ± 1.8 eV, the entire bandwidth is above the oxygen K-edge threshold in vanadium oxide. To obtain a homogeneously illuminated image, no sharp absorption features should be present in this chosen excitation bandwidth. The silicon nitride parts remain dark, as shown in Fig. 1(D). The x-ray line focus extends across the entire Siemens star structure in the vertical. The sample is scanned in the horizontal with 1000 steps of 250 nm across the inner part of the Siemens star. At every position, the signal is acquired for 5 s (total measurement duration approximately 96 min, including overhead). Figure 1(C) shows a typical detector image of the fluorescence signal. The structure of the spokes is clearly visible. We highlight a region of interest, which

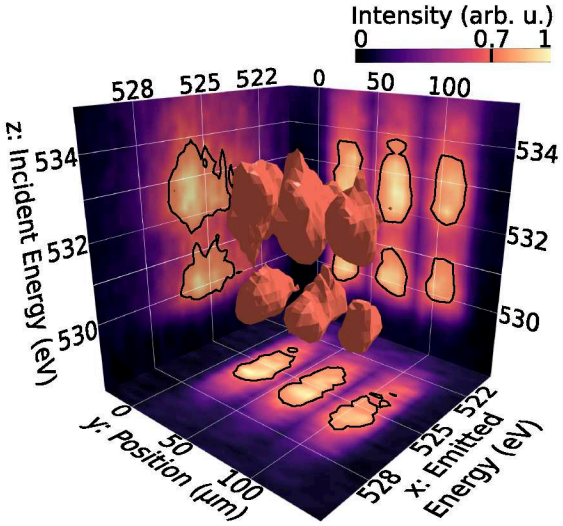

Fig. 2. Three-dimensional data set recorded in one monochromator scan and corrected for spaceenergy coupling. The microstructured sample, a group of three thin-film VO_2 squares with an edge length of 30 μm, is imaged along one dimension (here, y). Spatially resolved x-ray emission is recorded in-parallel (x, y plane), while the incident energy (z axis) is scanned. Shown are projections of the 3D data onto each plane, representing traditional RIXS maps (incident versus emitted energies) on the x, z plane, spatial maps of absorption spectra in the y, z plane, and spatial maps of emission spectra in the x, y plane. Isolines and surfaces for a relative intensity of 70% are shown, respectively, as a black line on the projection planes and in a pseudo-3D representation.

is set around the best focus on the detector. The signal within this area is averaged along the x direction, yielding the signal for that particular position of the x-rays on the sample {see the dotted line in the reconstruction [Fig. 1(D)]}. This procedure is repeated for every position of the x-ray line focus on the sample resulting in the final reconstruction [Fig. 1(D)].

Fourier ring correlation [23,24] is used to determine the spatial resolution of the RIXS-imaging setup. The correlation of spatial frequencies from two independently recorded images is quantified, and the crossover between signal and noise is determined. The obtained frequency corresponds to a spatial resolution of 1.8 μm.

Having established micrometer spatial resolution, we acquire RIXS maps from a sample that consists of a 50 nm thin VO_2 film on an Al_2O_3 substrate. The film is structured into squares with an edge length of 30 μm in groups of three with 10 μm spacing within the group and 90 μm spaces between groups. Consequently, the x-ray line focus extends over multiple microsquares in vertical imaging direction.

The monochromator is scanned across the oxygen K-edge excitations in VO_2 from 527 to 536 eV. Because of the bandwidth of ±1.8 eV, this scan has the effect that every point on the sample is illuminated by x-ray energies between 527 eV + 1.8 eV and 536 eV − 1.8 eV. Each recorded image contains spectral information of the emitted radiation in the horizontal (coordinate x). The signal in the vertical direction (along the focus line) originates from different positions on the sample (coordinate y), each excited by a slightly different incident energy, due to the monochromator dispersion.

The resulting dataset contains emitted intensities as a function of three coordinates: for every monochromator setting, one x, y-detector exposure is recorded. Accounting for the beamline

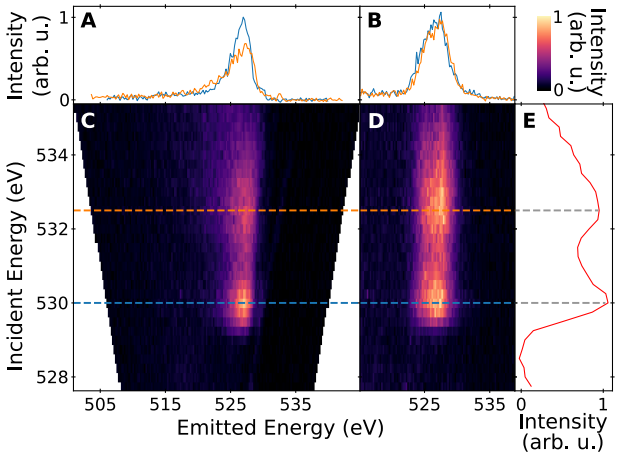

Fig. 3. (C), (D) RIXS maps created from an ∼11 μm (in the imaging dimension y) wide spot on a VO_2 thin film using an analyzer zone plate. (A), (B) RIXS spectra can be obtained by making cuts at fixed incident energies. For the acquisition of (A) and (C), the zone plate focuses elastic emission and moves along with the incident energy. For the acquisition of (B), (D), and (E), the analyzer zone plate focuses the constant-energy fluorescence emission. The trapezoid shape in (C) results from the corrected change of zone plate dispersion. (E) An absorption spectrum is obtained by averaging emitted energies.

dispersion, the vertical spatial sample coordinate y can be decoupled from the incident energy axis z. To visualize the corrected dataset, Fig. 2 shows the three projections of this 3D data onto 2D planes, as well as a 3D-isosurface of 70% relative intensity. RIXS maps showing x-ray emission depending on incident energy can be extracted from different positions of the illuminated sample by slicing this data set in the x, z plane. Furthermore, x, y and y, z slices, respectively, show the spatially dependent x-ray emission and partial fluorescence yield absorption data. In Fig. 3, RIXS maps taken from the center of the microsquares are shown. To increase statistics, the signal is averaged over ∼11 μm on the sample.

As already discussed above, the use of the AZP has the consequence that only a limited range of the emission spectrum is sufficiently focused at a time. For example, accepting a minimum energy resolution of 500 meV allows to use an emitted energy bandwidth $2\Delta E$ of approximately 1060 meV [see Eq. (2)]. To cover a larger emission energy range, the longitudinal AZP position needs to be adapted. This behavior necessitates different strategies when recording RIXS maps with the RIXS-imaging setup: focusing on fluorescence features at constant emission energy requires that the AZP is kept at a fixed position (Fig. 3D). To focus on constant energy transfer features instead, the AZP is scanned along with the incident energy, as shown in Fig. 3(C) for elastic emission. In the latter case, the movement is necessary to adapt the focal length of the AZP to the scanned incident energy. A consequence of the AZP movement is a change in its dispersion, which is compensated for in the data analysis (Fig. 3). Acquisition times for the data shown in Fig. 3 are discussed in Supplement 1.

The strategy to measure RIXS maps with the RIXS-imaging setup is different compared to conventional grating spectrometers, where a full RIXS spectrum from one point on the sample is measured without any scan and a RIXS map is recorded when scanning only the monochromator. With our setup, the strategy of acquiring a complete (one-dimensional) RIXS spectrum (at fixed excitation energy) in focus requires the AZP position to be scanned. However, this directly yields a full RIXS spectrum for every point on the sample, coupled to slightly different excitation energies (2D information). Measuring a 2D RIXS map with a large range of emission energies in focus therefore requires an independent scan of the monochromator and the AZP focus, which in turn directly yields 3D information, i.e., full RIXS maps for all positions along the illuminated part of the sample. The full advantages of parallelization in our setup are realized when RIXS maps for each point on the sample are to be recorded within a small range of emission energies. For such a scheme, the AZP can be kept fixed, and only the monochromator needs to be scanned.

Comparing the transmission zone-plate-based setup to reflection grating spectrometers, the performance parameters are quite similar: diffraction efficiencies can be optimized for both transmissive and reflective optics for certain energy ranges and are typically on the order of 10%–20% across the soft x-ray range. The achievable energy range is determined largely by the mechanical degrees of freedom. While reflection gratings are often corrected for optical aberrations within a limited energy range, the transmission zone plate is in principle a perfect optic and thus is not limited in the energy range. Practically though, the entrance and exit arm lengths as well as magnification considerations limit the range similarly. The collected solid angle of our AZP setup is 4×10^{-4} sr, which compares with grating collection angles on the order of 4×10^{-5} sr [14]. We stress though that our setup is very forgiving towards angular misalignment of several degrees, while reflection gratings, typically operated at about 2° grazing incidence angle, are very sensitive in this respect [12–15].

Our setup aims at a parallel acquisition at the cost of the narrower emission energy bandwidth that is properly imaged on the detector. In the future, this bandwidth can be increased by using a radially smaller AZP (at the expense of acceptance angle). For instance, reducing the zone plate width from the present 3 to 1.5 mm while keeping the outer radius fixed would result in a substantial reduction in average energy, broadening from 0.94 to 0.37 eV per 1 eV deviation from the energy that is focused (i.e., to about 40%), whereas reducing the size of the aperture of the zone plate reduces the accepted solid angle only to 50%. Depending on experimental requirements, an optimization is possible and can also be chosen *in situ* with movable apertures close to the AZP.

4. SUMMARY

In summary, we demonstrate RIXS measurements with a spatial resolution down to 1.8 μm with our RIXS-imaging setup based on an off-axis Fresnel zone plate. This measurement technique provides the additional ability to utilize the entire dispersed undulator harmonic without compromising the energy resolution of the spectrometer. As opposed to conventional spectrometers, we can use an x-ray focus line of nearly 1 mm length for efficient in-parallel recording of spatial and spectral information while maximizing the photon flux on the sample and partially compensating for naturally low soft x-ray RIXS cross-sections.

Funding. H2020 Marie Skłodowska-Curie Actions (701647); Helmholtz Association (VH-NG-1105).

Acknowledgment. We acknowledge DESY (Hamburg, Germany), a member of the Helmholtz Association HGF, for the provision of experimental facilities. Parts of this research were carried out at PETRA III, and we thank Kai Bagschik, Florian Trinter, and Frank Scholz for assistance in using beamline P04. FD received funding from the EU-H2020 Research and Innovation Programme under the Marie Skłodowska-Curie.

Disclosures. The authors declare no conflicts of interest.

Supplemental document. See Supplement 1 for supporting content.

REFERENCES

1. B. Keimer and J. E. Moore, "The physics of quantum materials," Nat. Phys. **13**, 1045–1055 (2017).
2. Y. Tokura, M. Kawasaki, and N. Nagaosa, "Emergent functions of quantum materials," Nat. Phys. **13**, 1056–1068 (2017).
3. E. Dagotto, "Complexity in strongly correlated electronic systems," Science **309**, 257–262 (2005).
4. G. Campi, A. Bianconi, N. Poccia, G. Bianconi, L. Barba, G. Arrighetti, D. Innocenti, J. Karpinski, N. D. Zhigadlo, S. M. Kazakov, M. Burghammer, M. V. Zimmermann, M. Sprung, and A. Ricci, "Inhomogeneity of charge-density-wave order and quenched disorder in a high-Tc superconductor," Nature **525**, 359–362 (2015).
5. R. German, B. Zimmer, T. C. Koethe, A. Barinov, A. C. Komarek, M. Braden, F. Parmigiani, and P. H. van Loosdrecht, "Temperature dependent percolation mechanism for conductivity in $Y_{0.63}Ca_{0.37}TiO_3$ revealed by a microstructure study," Mater. Res. Express **5**, 126101 (2018).
6. H. S. Choi, J. S. Ahn, J. H. Jung, T. W. Noh, and D. H. Kim, "Mid-infrared properties of a film near the metal-insulator transition," Phys. Rev. B **54**, 4621–4628 (1996).
7. M. M. Qazilbash, A. Tripathi, A. A. Schafgans, B.-J. Kim, H.-T. Kim, Z. Cai, M. V. Holt, J. M. Maser, F. Keilmann, O. G. Shpyrko, and D. N. Basov, "Nanoscale imaging of the electronic and structural transitions in vanadium dioxide," Phys. Rev. B **83**, 165108 (2011).
8. J. Laverock, S. Kittiwatanakul, A. Zakharov, Y. Niu, B. Chen, S. A. Wolf, J. W. Lu, and K. E. Smith, "Direct observation of decoupled structural and electronic transitions and an ambient pressure monocliniclike metallic phase of VO_2," Phys. Rev. Lett. **113**, 216402 (2014).
9. L. Vidas, C. M. Günther, T. A. Miller, B. Pfau, D. Perez-Salinas, E. Martínez, M. Schneider, E. Gührs, P. Gargiani, M. Valvidares, R. E. Marvel, K. A. Hallman, R. F. Haglund, S. Eisebitt, and S. Wall, "Imaging nanometer phase coexistence at defects during the insulator-metal phase transformation in VO_2 thin films by resonant soft x-ray holography," Nano Lett. **18**, 3449–3453 (2018).
10. A. Kotani and S. Shin, "Resonant inelastic x-ray scattering spectra for electrons in solids," Rev. Mod. Phys. **73**, 203–246 (2001).
11. L. J. Ament, M. van Veenendaal, T. P. Devereaux, J. P. Hill, and J. van den Brink, "Resonant inelastic x-ray scattering studies of elementary excitations," Rev. Mod. Phys. **83**, 705–767 (2011).
12. V. N. Strocov, "Concept of a spectrometer for resonant inelastic x-ray scattering with parallel detection in incoming and outgoing photon energies," J. Synchrotron Radiat. **17**, 103–106 (2010).
13. C. H. Lai, H. S. Fung, W. B. Wu, H. Y. Huang, H. W. Fu, S. W. Lin, S. W. Huang, C. C. Chiu, D. J. Wang, L. J. Huang, T. C. Tseng, S. C. Chung, C. T. Chen, and D. J. Huang, "Highly efficient beamline and spectrometer for inelastic soft x-ray scattering at high resolution," J. Synchrotron Radiat. **21**, 325–332 (2014).
14. T. Warwick, Y. D. Chuang, D. L. Voronov, and H. A. Padmore, "A multiplexed high-resolution imaging spectrometer for resonant inelastic soft x-ray scattering spectroscopy," J. Synchrotron Radiat. **21**, 736–743 (2014).
15. Y. D. Chuang, X. Feng, P.-A. Glans-Suzuki, W. Yang, H. Padmore, and J. Guo, "A design of resonant inelastic x-ray scattering (RIXS) spectrometer for spatial- and time-resolved spectroscopy," J. Synchrotron Radiat. **27**, 695–707 (2020).
16. Y. Shvyd'ko, "Theory of angular-dispersive, imaging hard-x-ray spectrographs," Phys. Rev. A **91**, 053817 (2015).
17. F. Marschall, Z. Yin, J. Rehanek, M. Beye, F. Döring, K. Kubiček, D. Raiser, S. T. Veedu, J. Buck, A. Rothkirch, B. Rösner, V. A. Guzenko, J. Viefhaus, C. David, and S. Techert, "Transmission zone plates as analyzers for efficient parallel 2D RIXS-mapping," Sci. Rep. **7**, 8849 (2017).
18. F. Marschall, D. McNally, V. A. Guzenko, B. Rösner, M. Dantz, X. Lu, L. Nue, V. Strocov, T. Schmitt, and C. David, "Zone plates as imaging analyzers for resonant inelastic x-ray scattering," Opt. Express **25**, 15624–15634 (2017).
19. J. O. Schunck, "Combining resonant inelastic x-ray scattering with micrometer resolution to image electronic properties of quantum materials," Master's thesis (University of Hamburg, 2019).
20. M. Beye, R. Y. Engel, J. O. Schunck, S. Dziarzhytski, G. Brenner, and P. S. Miedema, "Non-linear soft x-ray methods on solids with MUSIX—the multi-dimensional spectroscopy and inelastic x-ray scattering endstation," J. Phys. Condens. Matter **31**, 014003 (2019).
21. J. Viefhaus, F. Scholz, S. Deinert, L. Glaser, M. Ilchen, J. Seltmann, P. Walter, and F. Siewert, "The variable polarization XUV beamline P04 at PETRA III: optics, mechanics and their performance," Nucl. Instrum. Methods Phys. Res. Sect. A **710**, 151–154 (2013).
22. F. Döring, F. Marschall, Z. Yin, B. Rosner, M. Beye, P. Miedema, K. Kubicek, L. Glaser, D. Raiser, J. Soltau, V. Guzenko, J. Viefhaus, J. Buck, M. Risch, S. Techert, and C. David, "1D-full field microscopy of elastic and inelastic scattering with transmission off-axis Fresnel zone plates," Microsc. Microanal. **24**, 182–183 (2018).
23. M. van Heel and M. Schatz, "Fourier shell correlation threshold criteria," J. Struct. Biol. **151**, 250–262 (2005).
24. I. Mohacsi, I. Vartiainen, B. Rösner, M. Guizar-Sicairos, V. A. Guzenko, I. McNulty, R. Winarski, M. V. Holt, and C. David, "Interlaced zone plate optics for hard x-ray imaging in the 10 nm range," Sci. Rep. **7**, 43624 (2017).